The Planetary Science Journal, 3:144 (16pp), 2022 June https://doi.org/10.3847/PSJ/ac6e5f

Rover-mounted Hydrated Mineral Detector for Mars Exploration: A Preliminary Report

Soon Sam Kim[1], Eddie Ng[2], Jeongil Oh[1,6], Yahya Rahmat-Samii[3], Yubin Cai[3,4], and David Paige[5]
[1] Propulsion, Thermal and Materials Engineering Section, Jet Propulsion Laboratory, California Institute of Technology, Pasadena, CA 91109, USA
Soonsam.Kim@jpl.nasa.gov
[2] A Star Technologies, 1015 Doyle Place #2, Los Angeles, CA 90012, USA
[3] Department of Electrical Engineering, University of California, Los Angeles, CA 90095, USA
[4] MIT Media Lab, 20 Ames Street, E15-468 Cambridge, MA 02142, USA
[5] Department of Earth, Planetary, and Space Sciences, University of California, Los Angeles, CA 90095, USA
Received 2021 December 16; revised 2022 May 5; accepted 2022 May 10; published 2022 June 23

Abstract

The rover-mounted hydrated mineral detector (HMD) is based on a dielectric spectrometer (tuned frequency range of 0.8–4 MHz) that will detect bulk subsurface hydrated minerals in local scale. The HMD is a compact, low-mass (1.5 kg), and low-power instrument (5 W) suitable for Mars application. Compared with orbiter-based instruments with low horizontal resolution (5–10 km), the HMD will offer high resolution (2 m) that can identify optimal sampling sites for the presence of hydrated minerals. From field testing with reduced radio frequency (RF) power ($P_{rf} = 10$ mW), the HMD demonstrated detection of shallow buried gypsum samples. When developed with full RF power, the HMD could potentially detect hydrates down to depths of 2 m ($P_{rf} = 1$ W) or 4 m ($P_{rf} = 36$ W) in Martian soil. Unlike conventional dielectric spectrometers, which require small amounts of the sample (5–10 g) to be placed inside sample cells, the HMD will detect hydrated minerals by scanning over the Mars surface mounted on a rover platform (<1 m above ground) without any sample preparation. This capability will allow future rovers to rapidly assess the scientific potential of field sites. Compared with optical techniques that are limited to surface exposed mineralogical features that could be obscured by dust and weathering products, the HMD will detect bulk subsurface hydrated minerals along the rover traverse irrespective of surface obscuration. The HMD (TRL 4) is a proof-of-concept instrument that can be developed and matured for future Mars rover missions.

Unified Astronomy Thesaurus concepts: Space vehicle instruments (1548)

1. Introduction

1.1. Mars Hydrated Minerals

An overarching theme of NASA exploration is the search for extraterrestrial life, present or past, on Mars and other planetary bodies. Water ice exists on Mars in polar areas and may exist in the subsurface at moderate latitudes in some localities. Since water is regarded as a necessity of life, a recurring NASA theme for exploration has been "follow the water." Hence, a major element of NASA planetary missions has been the search for H_2O, whether in the form of mineral hydrates or water ice.

Orbital and landed mission results revealed widespread deposits of hydrated minerals formed in the presence of liquid water. Currently available evidence suggests that hydrated minerals on Mars are localized in sedimentary deposits that formed ~3 billion yr ago. They reinforce the conclusion that ancient Mars was warmer and wetter than it is today and increase the number of promising localities to search for evidence of past life.

Orbital observations, such as those of the Observatoire pour la Mineralogie, l'Eau, les Glaces, et l'Activité (OMEGA) instrument on board the Mars Express orbiter (ESA 2003), obtained visible and near-infrared (IR) spectra of the Martian surface materials. The OMEGA results (Arvidson et al. 2005; Bibring et al. 2005; Gendrin et al. 2005; Langevin et al. 2005a, 2005b; Mustard et al. 2005) show evidence for multiple localized ancient sedimentary deposits containing abundant sulfate minerals. The OMEGA visible–IR spectrometer identified hydrated sulfates through their distinct vibrational overtones involving water and hydroxyl in the 1–2.5 μm region in a variety of locations: within Valles Marineris and in Aram Chaos, essentially in association with light-toned layered deposits (Gendrin et al. 2005), and as large regional units in Terra Meridiani (Arvidson et al. 2005) and close to the perennial northern polar cap (Langevin et al. 2005a, 2005b). Notably, within the Valles Marineris, Juventae Chasma is a 2.5 km high and ~40 km long layered deposit, and OMEGA identified gypsum dominating in the layered strata and kieserite (Bibring et al. 2005). The Mars Reconnaissance Orbiter Compact Reconnaissance Imaging Spectrometer for Mars instrument has also detected a number of ancient regions containing hydrated silicate minerals (Mustard et al. 2008).

Surface observations, such as the Mars Exploration Rover Opportunity Rover results, show evidence for widespread exposures of sedimentary rocks in the Terra Meridiani region with high concentrations of hydrated minerals, such as kieserite, bassanite, and the iron sulfate mineral jarosite, whose average abundances are estimated to be on the order of 10 wt% (Christensen et al. 2004; Klingelhöfer et al. 2004; Morris et al. 2005). Results of the Miniature Thermal Emission Spectrometer (Mini-TES) on the Opportunity investigation at the Meridiani Planum show that sulfates of aqueous origin are present in all of the outcrops in volume abundances of 15%–35% and sheet silicates of 10%–20% at some of the outcrops (Christensen et al. 2004). The sulfates they used to fit to the Mini-TES spectral data included gypsum ($CaSO_4 \cdot 2H_2O$),

[6] Current address: Naval Information Warfare Center Pacific (NIWC Pacific), 53560 Hull Street, San Diego, CA 92152, USA.

bassanite ($2CaSO_4 \cdot H_2O$), epsomite ($MgSO_4 \cdot 7H_2O$), kieserite ($MgSO_4 \cdot H_2O$), glauberite [$Na_2Ca(SO_4)_2$], and jarosite [$KFe_3(SO_4) \cdot 2(OH)_6$] species. They found that the best fit was consistently provided by the Mg and Ca sulfates. Morris et al. (2005) calculated average abundances of sulfates; kieserite at 12–23 wt% and bassanite at 8 wt%, respectively.

The Mars Science Laboratory Curiosity rover payload detected unequivocal evidence for hydrated minerals. The X-ray diffraction analyses by the CheMin (Chemistry & Mineralogy) found abundant clay minerals (phyllosilicates; Blake & the MSL Science Team 2013). The Sample Analysis at Mars instrument heated samples to 800°C and detected H_2O, indicating the presence of hydrated minerals such as phyllosilicates and sulfates (Mahaffy & the MSL Science Team 2013). These are consistent with the interpretation that this site once hosted a potential environment for microbial life.

Existing and ongoing orbital and surface observations have made a strong case for the presence of widespread hydrated minerals on Mars. From Mars Odyssey neutron spectrometer and OMEGA visible and near-IR data, Wernicke & Jakosky (2021) estimated that the volume of water stored in the form of Martian hydrated minerals is about seven times larger than the volume of water stored in the polar caps and near-surface ice; i.e., the hydrated minerals are a significant source for Martian water. They determined that the volume of water stored in the form of hydrated minerals on Mars is 130–260 m global equivalent layer (GEL) and possibly extends from 70 to 860 m GEL, which amounts to the thickness of water if it were spread evenly over all of Mars.

For missions that will employ drilling and digging for subsurface sample collection, the availability of a method for detecting and characterizing subsurface hydrated minerals will be especially valuable. Unfortunately, we presently have no data regarding the possible distribution of hydrated minerals on Mars at depths below 1 m. According to observations by Pan et al. (2017), hydrated/hydroxylated minerals are detected more frequently in large craters, consistent with the scenario that the hydrated minerals are being excavated from deep basement rocks. Determination of the abundance of hydrated minerals in the subsurface is particularly important for future missions. It is likely that the currently exposed hydrated minerals represent a small fraction of those that are actually present (Vaniman et al. 2004; Bibring et al. 2005).

According to Schopf et al. (2012), evaporitic sulfate minerals represent a promising target in the search for evidence of past life on Mars. With samples of gypsiferous deposits from several locations on Earth, they found diverse fossil microscopic organisms permineralized in primary bottom-nucleated gypsum samples. Likewise, they expected that such evaporates on Mars would contain permineralized microfossils if life ever arose on Mars. On Earth, it is well established that diverse microorganisms are able to thrive in highly saline gypsum-precipitating environments (Oren et al. 2009) and metabolize biologically available sulfate. Several authors (Stivaletta & Barbieri 2009; Wierzchos et al. 2006; Dong et al. 2007; Allwood et al. 2013; Cámara et al. 2016; Vítek et al. 2016) reported the presence of microbial endoliths in translucent gypsum crystals and soil grains of samples on Earth, as well as hydrated Mg minerals (Balci et al. 2020) and conjectured as analogs of a possible extant or past Martian biota.

Determining the abundance of hydrated minerals in the subsurface is particularly important for future in situ resource utilization (ISRU) applications. Hydrates represent a potentially important source of extractable water, particularly in low-latitude regions where models predict that subsurface temperatures are too high to permit the stability of water ice. The Mars water ISRU study led by Abbud-Madrid et al. (2016) states that polyhydrated sulfates are the preferred water sources equatorward of 50° latitude. A natural concentration of polyhydrated sulfate minerals such as gypsum would involve the lowest mass of raw material and have lower power requirements. Compared with clay mineral deposits, the polyhydrated sulfates would have both a lower decomposition temperature and a higher water content. Water can be extracted from hydrates by heating under Martian atmospheric conditions (Boynton et al. 2001).

Since it is likely that most human exploration activities will be concentrated in the low- and mid-latitude regions of Mars, hydrates are likely to be a key focus of robotic precursor missions.

Unlike remote sensing of exposed hydrated minerals by orbiter-based visible and near-IR with kilometer-scale resolution, the rover-mounted hydrated mineral detector (HMD) will offer local characterization of the presence of subsurface hydrates with high resolution (2 m) and guide sampling at the landing sites. From field testing with reduced radio frequency (RF) power (10 mW), the HMD demonstrated the detection of shallow buried gypsum samples (Section 3). When developed with full RF power (1 W), the HMD has the potential to detect hydrates down to depths of 2 m in Martian soil.

1.2. Dielectric Spectroscopy

Dielectrics are insulating materials with negligible or small electrical conductivity. Characterization of dielectrics subject to time-varying electric fields, $E(t)$, is the objective of dielectric spectroscopy (Meakins 1961). The imposition of an external electric field produces a slowly varying dielectric polarization without significant charge transport. Dielectric polarization can be regarded as sum of two terms, $P = P_i + P_o$, where P_i is the induced polarization (temperature-independent) caused by the separation of positive and negative charges due to the action of the electric field, and P_o is the orientation polarization caused by the preferential alignment of permanent dipoles in the direction of the electric field. Even in the absence of an applied electric field, water is a polar molecule with a permanent dipole moment, $\mu = 1.854$ D, due to an inherent asymmetry within the molecular structure.

The frequency-dependent dielectric properties of materials can be represented by a complex electrical permittivity, $\epsilon = \epsilon' - j\epsilon''$, in which the real part of the permittivity, ϵ', is a measure of the polarizability of the material constituents. The imaginary part of the permittivity, ϵ'', represents the energy absorption from the applied electric field, E. The energy transfer is expressed as the dielectric loss factor, $\tan\delta = \epsilon''/\epsilon'$. The resultant dielectric spectra can be characterized from very low frequencies up to IR range. The orientation polarization P_o occurs only in materials with a permanent dipole moment, such as water. The dielectric response arises from a torque, $\tau = \mu \times E$, exerted by a polar molecule with an electric dipole moment μ in the presence of a radiation field $E(t)$. The torque tends to turn the molecule along the direction of the field, but this turning is opposed by the inertia of rotating molecules and their interaction with neighboring molecules. With increasing frequency, the molecules become too slow to follow fast alternating electric fields, and ϵ' will decrease to lower values

(ϵ'_∞). Thus, dielectric relaxation is a delayed response of a material to a changing stimulus, and the time lag between the electric field and polarization implies an irreversible degradation of free energy to heat. The frequency at which ϵ' has decreased to half its lower-frequency value (static dielectric constant, ϵ'_0) is called the relaxation frequency. At this frequency, the dielectric energy loss, ϵ'', or dielectric absorption is at maximum.

With the limited tuned RF scan range of the HMD (0.8–4 MHz), the dielectric absorption (ε'') is monitored at the relaxation frequency rather than dispersion (ε') for the detection of hydrates. Hydrates show unique dielectric absorption (ϵ'') at 1–3 MHz, and there is no need to deduce complex permittivity ($\epsilon = \epsilon' - j\epsilon''$) for the detection. This provides advantages, as there is no need to acquire true baselines (ϵ'_0 or ϵ'_∞) for each component, which is difficult for mixed samples.

There are several physical forms of water: free water, adsorbed water, and bound water. With bound water, such as in hydrated minerals, the reorientational motion of H_2O will manifest itself as dielectric absorption and can be detected through the measurement of the RF absorption (positively correlated with ϵ'') as a function of frequency. The absorption is proportional to the abundance of dipoles in the samples and the dipole moment values of the molecules involved. Thus, the dielectric absorption depends on the extent of hydration, providing an indicator of the water content and its structural relationships in the host material.

For the HMD, the frequency range commonly investigated is below a few gigahertz, e.g., 0.8–4 MHz, where the dielectric response is dominated by orientational polarization processes, and the observed dielectric loss, ϵ'', is due to polarization lag. For hydrated mineral detection, the HMD is focused on the detection of changes in ϵ'' by monitoring RF absorption during frequency scans.

In solids, the reorientational motion of the dipoles is hindered, separated by an energy barrier of ΔE_a, the rotational activation energy. With the application of an electric field, a small excess of dipoles will reorient into more favorable positions, thus giving rise to dielectric absorption. The temperature dependence of the frequency of maximum absorption, $f_{\max}$, can be estimated from the Arrhenius equation, $f_{\max} = A \exp(-\Delta E_a/RT)$. Thus, depending on the magnitude of ΔE_a, the dielectric absorption maximum will shift to a lower frequency under Martian conditions, e.g., 220 K, as shown in Figure 1. However, due to the complex nature of the relaxation processes, the temperature dependence and the degree of frequency shift are strongly affected by the water content and the nature of hydration, with bound water in hydrated minerals showing little shift (200–290 K), unlike the ice or clay cases, as shown in Figure 1.

1.3. Dielectric Spectra of Mineral Samples

Variable-temperature dielectric spectra of representative hydrated minerals, as well as ice samples, were measured by a laboratory dielectric spectrometer (Novocontrol), as shown in Figure 1. The data were obtained by Prof. Jovan Mijovic, Polytechnic Institute of New York University, through a JPL Subcontract (2006). Mineral samples were ground into a powder and pressed into a pellet inside a sample cell (10 mm diameter × 1 mm thick cylinder), and dielectric spectra were obtained from 290 to 200 K.

Dielectric spectra of the representative Martian hydrates gypsum ($CaSO_4 \cdot 2H_2O$), kieserite ($MgSO_4 \cdot H_2O$), anhydrite ($CaSO_4$), bassanite ($CaSO_4 \cdot 0.5H_2O$), hexahydrite ($MgSO_4 \cdot 6H_2O$), and epsomite ($MgSO_4 \cdot 7H_2O$) are shown in Figure 1. With little temperature dependence, they all show an absorption maximum at 1–3 MHz, decreasing to a baseline value at >100 MHz (Figures 1(C) and (D)). The HMD tuned scan ranges (0.8–4 MHz) will cover the RF absorption. Notice, in Figure 1(D), the decrease of the measured absorption (permittivity ϵ'' values) as the water contents decrease from gypsum to kieserite to anhydrite. The absorption (ϵ'') at 1–3 MHz is used for their detection. The HMD detects the hydrates as a whole, primarily not distinguishing individual hydrates.

A dielectric spectrum of Martian simulant soil, JSC Mars-1 (Allen et al. 1998), was obtained at 220 K, as shown in Figure 1(E). The JSC Mars-1 does not contain any hydrated minerals (see note under Allen et al. 1998) but shows high absorption, $\varepsilon'' = 0.15$–0.22, compared with that of the hydrated minerals ($\epsilon'' = 0.05$–0.17).

Detecting the presence of gypsum in mixtures with high-RF absorbers such as JSC Mars-1 can be achieved by signal processing and application of higher RF power, if necessary. As a demonstration, a simulation for signal processing with frequency modulation (FM) is shown in Figure 2. An equal-volume mixture of JSC Mars and gypsum is used for the simulation. By FM/demodulation signal processing (Section 2.3), the HMD obtains a derivative ($d\varepsilon''/df$) of the absorption spectrum, $\varepsilon''(f)$ (e.g., Grum et al. 1972; Dubrovkin 2021). By derivative signal processing, any constant absorption (DC component) is filtered out, and only the changes of absorption as a function of RF, $d\varepsilon''/df$, are emphasized as a signal. For mixed signals, it is easier to distinguish the presence of gypsum in derivative form than in absorption. Thus, as long as gypsum has a unique absorption peak that is not overlapped with others, such as JSC Mars, it can be sorted out from the mixed derivative signal. The FM is an essential part of the signal-processing scheme to improve the quality of the signal over the background noise (Section 2.3).

The HMD detection is made by monitoring variations in dielectric absorption over the HMD scan ranges along the rover traverse (Section 3). Thus, any absorption always present during the traverse, e.g., Mars soil, can be regarded as background and subtracted out.

Another high-RF absorber, clay has a large monotonically decreasing absorption from $\varepsilon'' = 5.5$ to 2.2 with no characteristic peak (Figures 1 and 2(C)). During traverse, when the HMD would detect a sharp increase of background absorption, it could be construed as an encounter with claylike material. The presence of material with high absorption will affect RF penetration depth into the soil, thus results in shallower probing in search of subsurface hydrates, or require higher RF power for the HMD operation.

Unlike hydrated minerals (bound water), the dielectric absorption frequency of free water (ice) or adsorbed water (clay) depends strongly on temperature (Figures 1(A) and (B)). For ice, the frequency shift is from 10 Hz to 10 kHz at Martian temperatures from 200 to 268 K. Such low frequencies (<10 kHz) will require too large an antenna sensor structure (e.g., at 1 kHz, wavelength $\lambda = 300$ km) to be deployed by the HMD.

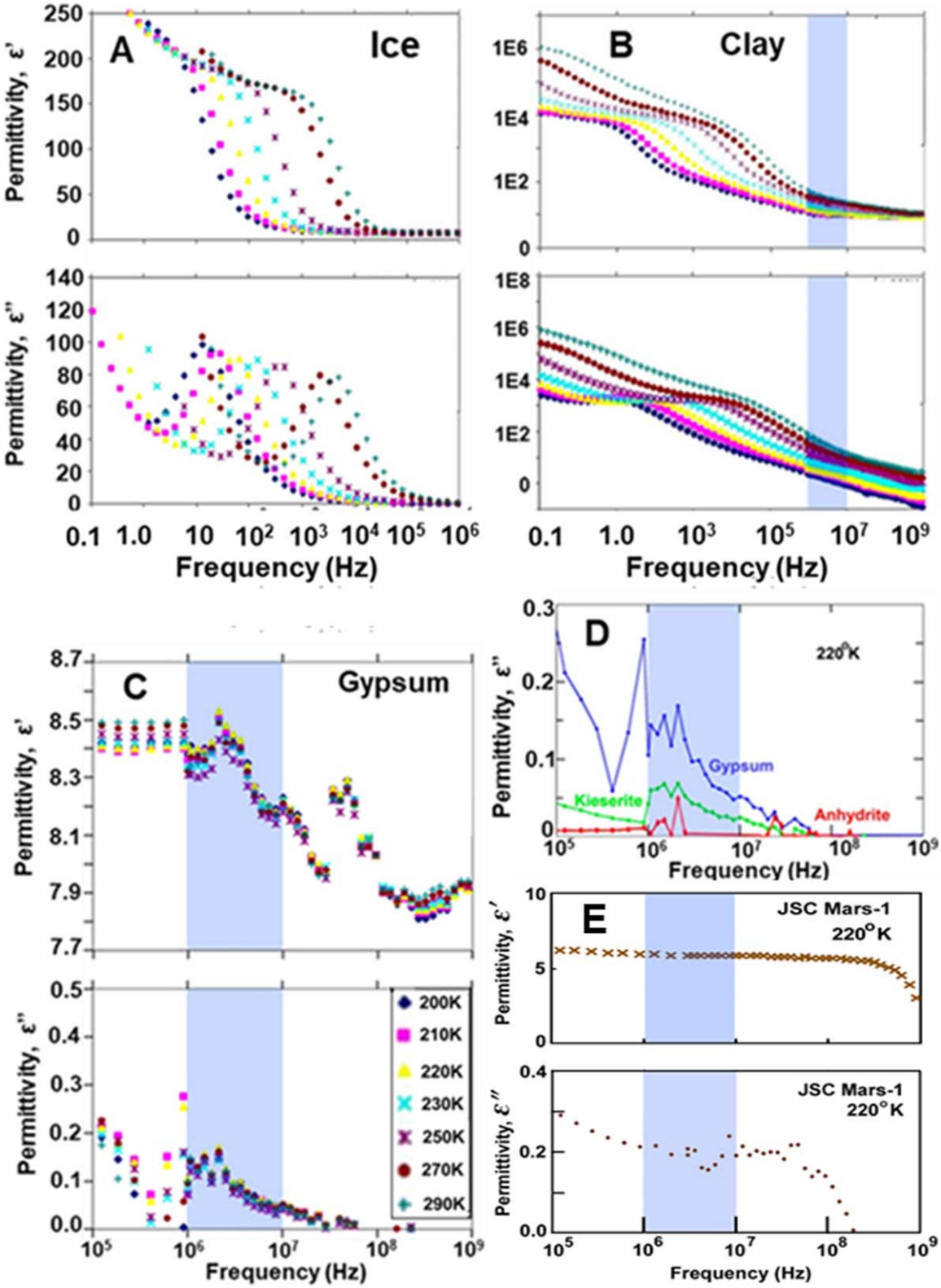

Figure 1. Dielectric spectra of minerals from 200 to 290 K. (A) Ice. (B) Montmorillonite clay. (C) Dielectric spectra (ϵ'' vs. frequency) of gypsum ($CaSO_4 \cdot 2H_2O$). Notice that there is little temperature dependence in the absorption maximum. The frequency range of interest, 1–10 MHz, is shaded in blue. (D) Dielectric spectra of representative hydrate minerals on Mars: gypsum ($CaSO_4 \cdot 2H_2O$), kieserite ($MgSO_4 \cdot H_2O$), and anhydrite ($CaSO_4$) at 220 K. Notice that the magnitude of absorption follows the water contents of hydrates. (E) Dielectric spectra of Mars simulant soil, JSC Mars-1 at 220 K. (The dielectric spectra were obtained by Prof. Jovan Mijovic, Polytechnic Institute of New York University through a JPL Subcontract, 2006.)

Conventional laboratory dielectric spectrometers, e.g., Novocontrol Technologies (Frankfurt, Germany) and Dielectric Probe (Keysight Technologies, Santa Rosa, CA), require small amounts (5–10 g) of samples placed inside a sample cell for the measurements. The HMD does not require sampling; rather, it will be mounted on a rover (0.3–1 m above ground) and detect

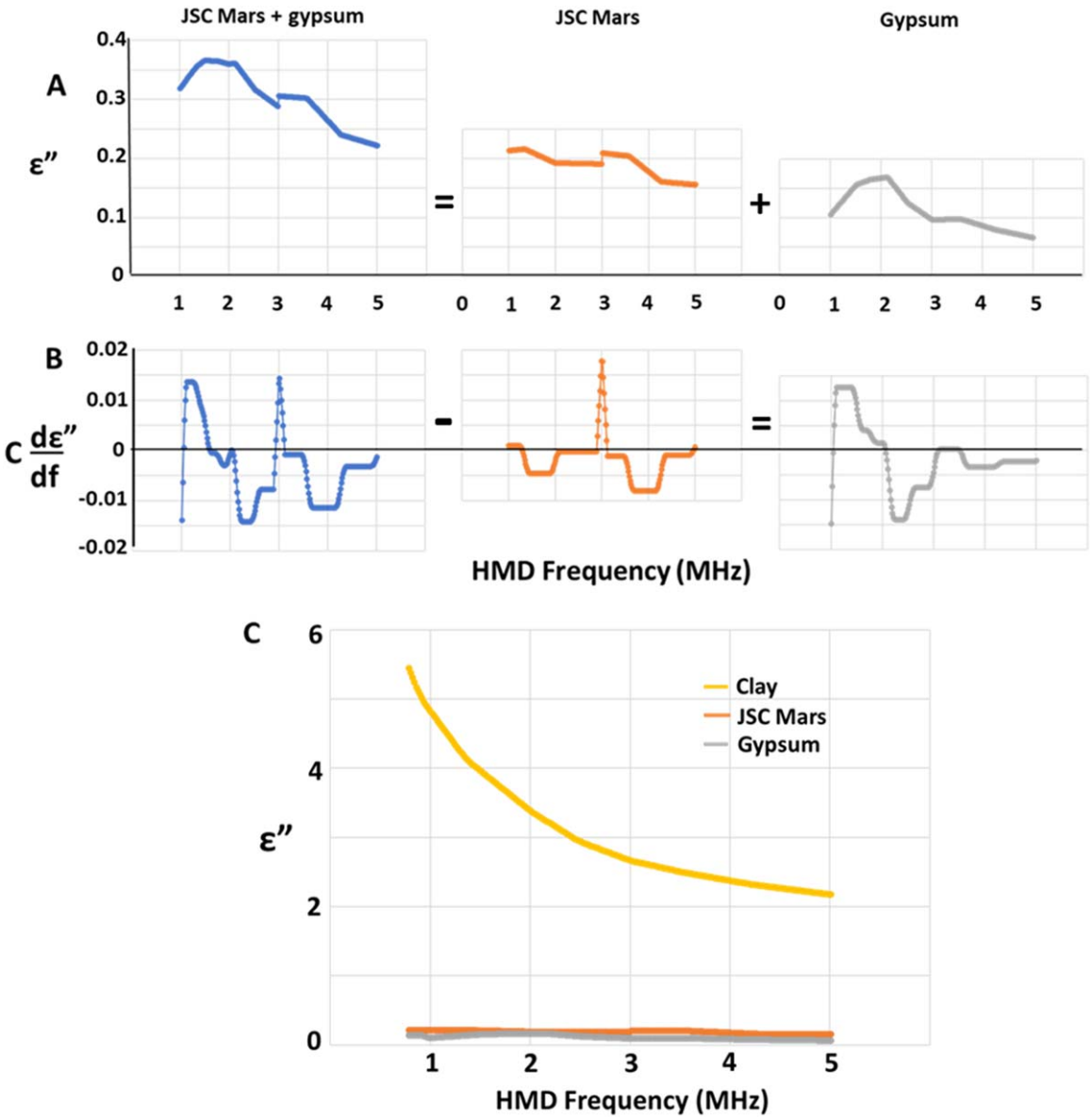

Figure 2. (A) and (B) Simulation of an equal-volume mixture of gypsum and JSC Mars-1 soil using the data from Figure 1 at 220 K. (A) Plot of the dielectric absorption, $A(f)\alpha\epsilon''(f)$, of the individual component and the mixture as a function of frequency. (B) Derivative ($cd\epsilon''/df$) of the mixture and components (c is a constant). The derivative of absorption is obtained by FM (Section 2.3) of the absorption signal shown in panel (A). This demonstrates that through FM/demodulation signal processing, any constant absorption (DC component) is removed, and the changes of absorption as a function of RF are emphasized and obtained as a signal. Thus, gypsum with characteristic absorption peaks in the 1–3 MHz region, it becomes easier to distinguish from the mixed signal, and by subtraction of JSC Mars component as a background produces the gypsum signal. (C) Comparison of absorptions by clay, JSC Mars, and gypsum (at 220 K; data from Figure 1).

the presence of hydrated minerals by scanning over the ground. This capability will enable fast evaluation of landing sites and locate sampling sites.

2. HMD Instrumentation

2.1. Antenna Sensor Structure

Originally, the antenna sensor was designed for a relatively wide range, 0.8–10 MHz. However, due to the limited availability of commercially available components, a hardware version was developed for a tuned frequency range of 0.8–4 MHz, which still includes the maximum RF absorption for hydrates (1–3 MHz). In this range, with free space wavelengths of $\lambda \approx 75$–375 m, devising a compact antenna sensor that is compatible with typical rover dimensions (e.g., 2 m × 1 m × 1 m high) is a challenging task. When the dimensions of a structure are much smaller than the half-wavelength, $\lambda/2$, the structure becomes more of a lumped circuit element, and most of the electromagnetic (EM) fields are confined to the vicinity of the structure rather than efficiently radiating like a conventional matched antenna. The HMD is primarily utilizing the near-field EM, and in this respect, the structure can be termed an antenna sensor. The design objective of the antenna sensor is to exert a maximum electric field (E) into the subsurface for the transmit side (Tx), and, due to the reciprocity of the antenna pattern, such a sensor structure will provide high sensitivity for detection of variation in coupled RF power for the receive side (Rx). The receive sensor will be sensitive to changes in RF absorption (ϵ'') as manifested by changes in the impedance of the circuit.

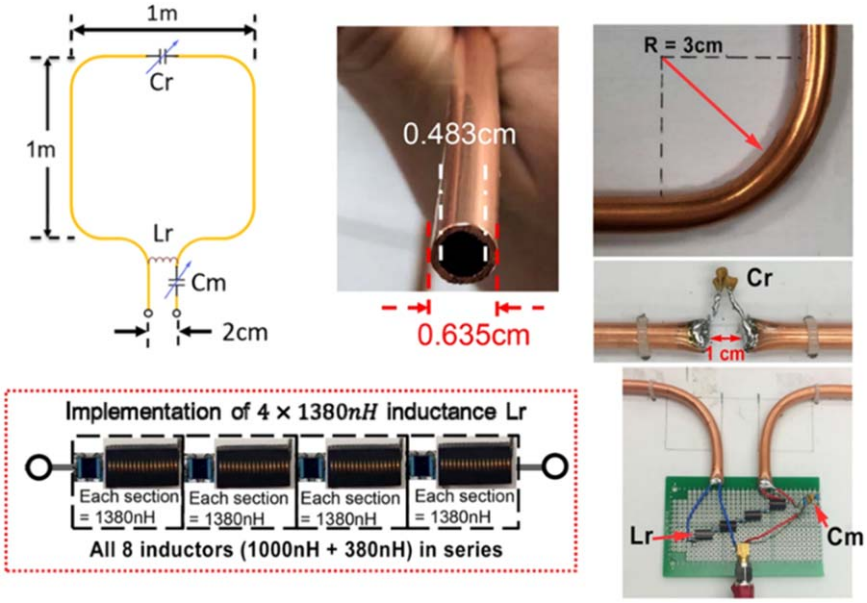

Figure 3. The HMD superquadric loop antenna sensor with copper tube construction: OD = 0.635 cm, ID = 0.483 cm, wall thickness = 0.076 cm. All the curvatures have a 3 cm radius. A set of discrete components (capacitors, Cr and Cm, and a fixed inductance, Lr = 4 × 1380 nH) is used for laboratory tests of the antenna sensor tuning.

As for the antenna sensor, a superquadric loop structure (Jensen & Rahmat-Samii 1994; Bellett & Leat 2003; Boswell et al. 2005) made of thin copper tubing was selected for the HMD and is shown in Figure 3. Figure 4 shows the H and E field distribution obtained by a high-frequency structure simulator and verified by integrating currents over the loop using Matlab.

The superquadric loop can be tuned to a resonance frequency with two sets of variable capacitors, Cr and Cm, and a fixed inductor Lr (Figure 3). Simulated Cr/Cm values using computer simulation technology (CST) are listed in Table 1 as a function of RF. The values are confirmed in the lab by placing discrete sets of corresponding capacitors into the antenna sensor. In the HMD instrument, the discrete capacitors are replaced by sets of digitally programmable capacitor arrays as described in Section 2.2.

The HMD system consists of two antenna sensors, transmit (Tx) and receive (Rx), in a bistatic mode (Figure 4). The EM wave from the Tx antenna sensor impinges on the soil surface (active system), and a significant portion of the energy is transmitted into the subsurface due to the relatively low frequency. The electric field (E) of the transmit antenna will interact with the water molecules (permanent dipoles) of the subsurface hydrated minerals, and any ensuing RF absorption can be detected by the Rx antenna sensor.

For the characterization of the EM field configuration, the CST EM solver program was also used, and the results are shown in Figures 4 and 5, e.g., in a plane 7 m below the antenna sensor (1 m above ground and 6 m depth in the soil) at RF power $P_{\rm rf} = 1$ W and a frequency of 1 MHz. In Figure 4(A), the E field pattern is for the Tx. As shown in the figure, the E field distribution is not symmetric with respect to the antenna sensor feed (indicated by Tx in Figure 4(A)). This is due to the localized nature of Cr/Cm/Lr. For example, the E fields are weaker at the feed side (intensity indicated green to blue) and much stronger on the opposite side of the feed (intensity indicated in red). In order to maximize the sensitivity between Tx/Rx, the antenna sensors are placed with their RF feeds away from each other, as shown in Figure 4(C). Thus, the Tx antenna will have a maximum E field opposite from the feed, and, due to the reciprocity of the antenna pattern (e.g., Kraus 1988), the Rx antenna will also have maximum E field receiving sensitivity opposite from the feed.

Figure 5 shows a simulation for the E field intensity from the Tx antenna sensor as a function of depth in the soil for three cases: case 1 with single-layer soil and cases 2 and 3 with two layers, e.g., soil ($\epsilon = 2.53$) and gypsum ($\epsilon = 3$) or soil and material with a higher dielectric constant ($\epsilon = 8.3$), respectively. Since the Tx antenna sensor is identical to the Rx antenna sensor, the receiving sensitivity at the Rx side is proportional to the E field intensity, as shown in Figure 5. The plot of the E field strength as a function of depth can be used as a rough estimate for the HMD detection depth at different RF powers. For example, the plot shows that at RF power $P_{\rm rf} = 1$ W, the E field at <1 m depth is 0.3 V m^{-1}, and at 2 m depth, it is 0.03 V m^{-1}. During field testing (see Section 3), the HMD RF power at the Tx side was attenuated to $P_{\rm rf} = 0.01$ W, so the HMD used an E field strength of 0.03 V m^{-1} ($E\alpha\sqrt{P_{\rm rf}}$; Equation (3)) to detect gypsum samples buried at <0.1 m depth. Alternately, from Figure 5(D), this field strength corresponds to an E field at ~2 m depth for the Tx with full RF power, $P_{\rm rf} = 1$ W. Thus, from the point of E field strength, gypsum buried at 2 m depth could be detected with $P_{\rm rf} = 1$ W.

2.2. Antenna Sensor Resonance Tuning

In order to achieve tuned RF scans (0.8–4 MHz), it is necessary to continuously maintain the antenna sensors (Tx/Rx) under resonance conditions. For this purpose, sets of digital programmable capacitor arrays (Digicap, e.g., NCD2400M, IXYS, Little Fuse, TX, USA) are used for Cr/Cm, replacing the discrete capacitors.

The Digicap is an integrated circuit device with the feature of adjustable capacitance (1.7–194 pF, code 0–code 511) across its output terminals when controlled over the inter-integrated circuit (I2C) interface. A block diagram for the antenna sensor

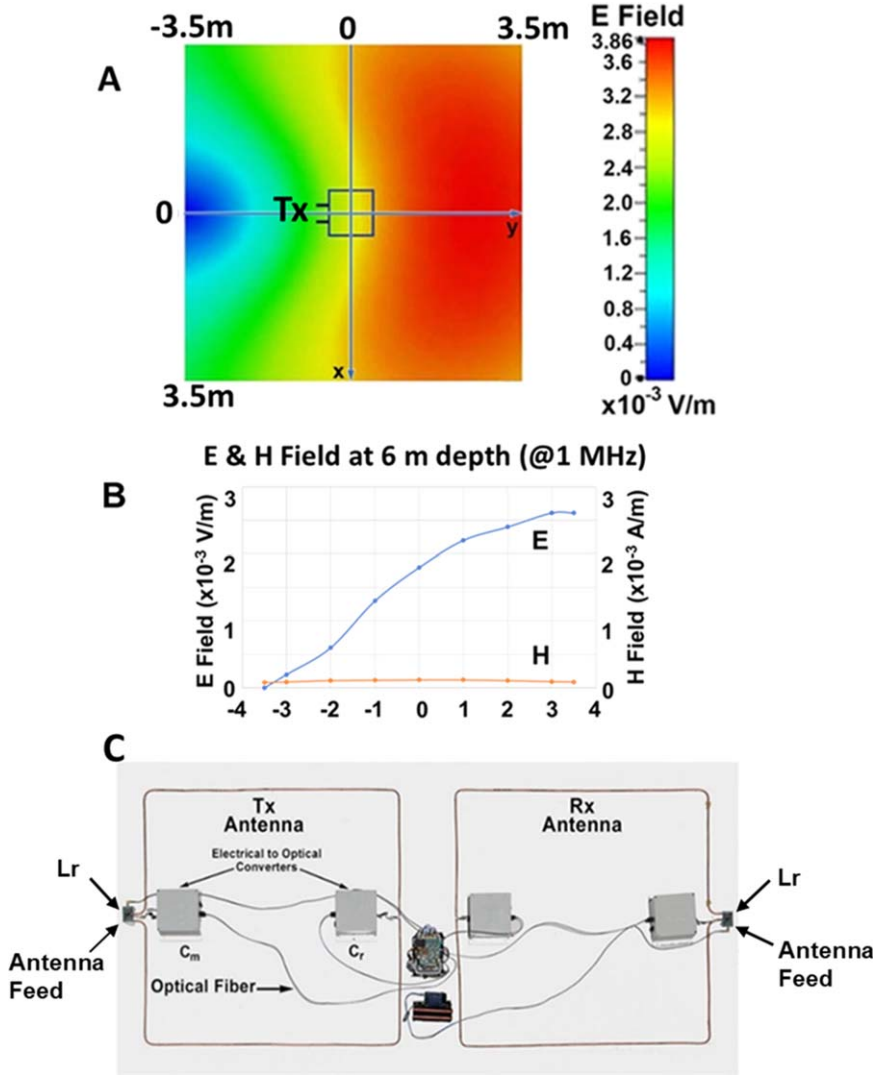

Figure 4. A CST simulation with localized capacitances and inductors, Cr/Cm/Lr, for E and H field intensity at 6 m depth into the soil (dielectric constant = 2.53) from a platform 1 m above the ground. RF, $f = 1$ MHz; RF power, $P_{rf} = 1$ W. (A) E field intensity in color plot. (B) E and H field intensity in numeric plot. (C) HMD antenna sensor configuration for field testing. Notice that the Tx/Rx antenna sensors are placed with the RF feeds away from each other. This is to maximize the E field overlap between the Tx/Rx antenna sensors and increase detection sensitivity. All electric wire connections are replaced with optical fibers in order to reduce the system capacitance for antenna sensor resonance tuning. The four gray boxes contain Cr and Cm resonance tuning circuits with rechargeable battery packs (5VDC).

Table 1
CST Simulated Tuning Capacitance Values of Cr and Cm with Fixed Inductance, Lr = 4 × 1380 nH, for the Frequency Ranges from 0.8 to 10 MHz[a]

	Target Freq. (MHz)	0.8	1	2	3	4	5	6	7	8	9	10
CST simulated values	Cr (pF)	3135	2141	530	225	118	70.5	44.8	28.7	17.5	10.3	5
	Cm (pF)	3964	2068	435.4	199.6	116.8	75.5	53.0	40.0	32.7	26.6	22.2
	Res. freq. (MHz)	0.82	1.00	2.00	3.00	4.00	5.01	6.00	7.01	8.00	9.00	10.00
Measured values[b]	Res. freq. (MHz)	0.815	0.994	1.996	2.94	3.94	4.87	5.88	6.87	7.89	8.72	9.64

Notes.
[a] Initially, antenna resonance tuning was planned for the whole frequency scan range (0.8–10 MHz), even though the limitations of the Digicap forced the tuned HMD range to 0.8–4 MHz.
[b] The measured resonant frequencies were obtained by using a combination of discrete fixed-element capacitors for Cr, Cm to meet the simulated values in the lab.

tuning circuit is shown in Figure 6. In an array, there are 12 Digicap devices, all connected in parallel, sharing the same I2C bus and contributing to the combined capacitance. There are four Digicap arrays (Tx Cr, Tx Cm, Rx Cr, and Rx Cm), and each of the four arrays shares the same design with the following components: internal power source, fiber optical receiver, microcontroller, and Digicap array (12× of NCD2400M). The Digicap arrays were programmed based on the Cr/Cm values listed in Table 1 and plotted in Figure 7(A).

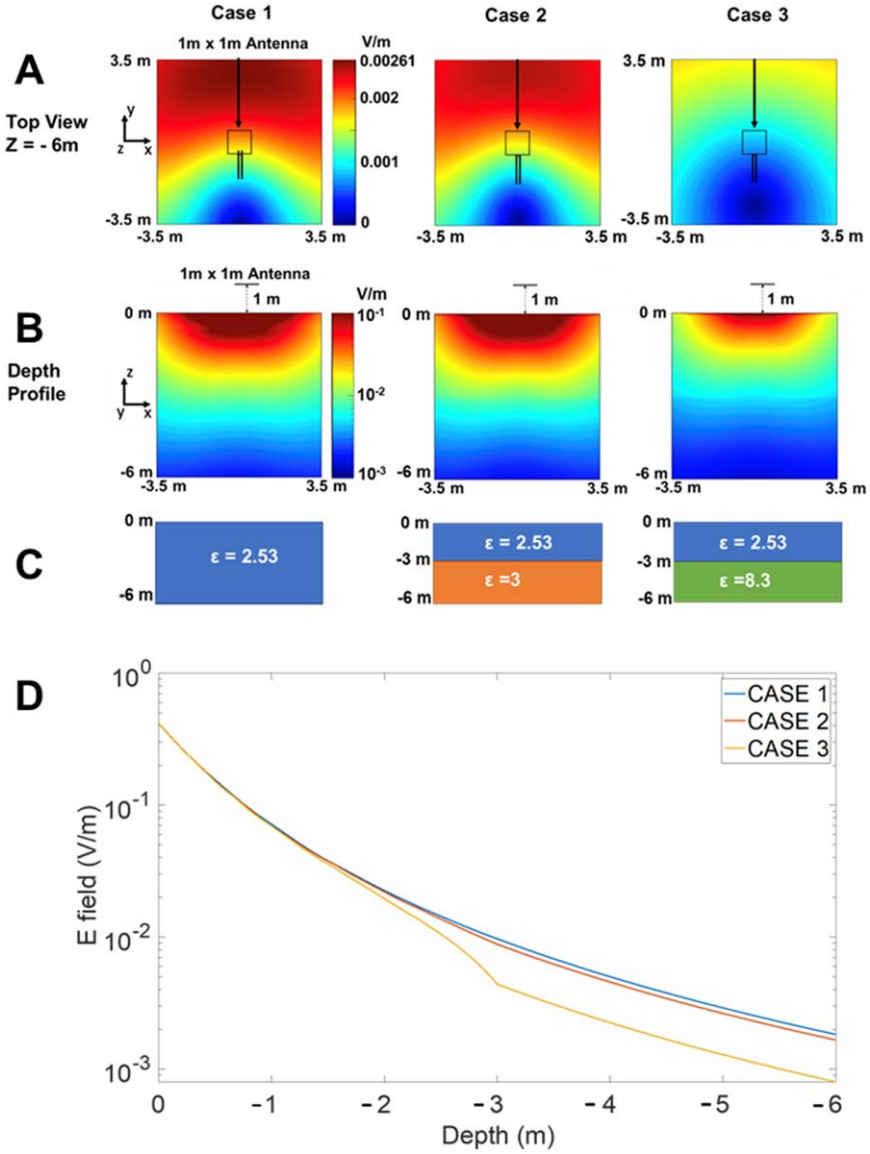

Figure 5. The CST simulation (CST Studio Suite 3D EM Simulation & Analysis Software) of electric field intensity with localized capacitances, Cr/Cm/Lr, at RF power $P_{rf} = 1$ W and RF $f = 1$ MHz for three soil layer cases. (A) E field intensity at 6 m depth into the soil from a platform 1 m above the ground. (B) E field distribution as a function of depth in the soil from the surface, 0 to −6 m. (C) Soil layer configurations: case 1, single layer with dielectric constant $\varepsilon = 2.53$; case 2, two layers with $\varepsilon = 2.53$ and 3; and case 3, two layers with $\varepsilon = 2.53$ and 8.3. (D) E field intensity as a function of depth for the three soil layers. For case 1, $P_{rf} = 1$ W, the E field at <0.1 m depth is 0.3 V m^{-1}. During field testing (see Section 3), the HMD RF power at the Tx side was attenuated to $P_{rf} = 0.01$ W, so the HMD used an E field strength of 0.03 V m^{-1} ($E\alpha\sqrt{P_{rf}}$) to detect gypsum samples buried at <0.1 m depth. Alternately, from panel (D), this field strength corresponds to the E field at ∼2 m depth when the Tx RF power $P_{rf} = 1$ W. When the RF power is increased, e.g., $P_{rf} = 36$ W, this E value ($E = 0.03$ V m^{-1}) corresponds at ∼4 m depth into Martian soil.

With the fabricated Digicap arrays, there appear to be inherent capacitance values added to the specified values; e.g., at code 0, the actual measurement shows 87.2 pF, whereas the data sheet shows 20.4 pF (=1.7 pF × 12). This added capacitance (66.8 pF) limits the high-frequency side of the RF scan, e.g., 7 MHz at 20.4 pF, whereas 4 MHz at 87.2 pF, resulting in the tuned RF scan range of 0.8–4 MHz. Another limitation in RF power comes from the Digicap. The HMD electronics produce a Tx RF power of 1 W; however, due to the low voltage limitation (<3.5 V) of Digicap, the Tx RF power is attenuated to 0.01 W.

In terms of communication flow, the desired capacitance value of each of the four Cm/Cr capacitor arrays is commanded by the HMD electronics through optical fibers. Each capacitor array responds to the command and makes the necessary adjustments to provide the requested capacitance value across the output terminals.

A rechargeable battery pack is used as an internal power source, providing stable 5VDC to all of the components in the Cm/Cr subsystem (Figure 6). An on/off switch is added to control the power flow. The fiber optics receiver in the Cm/Cr subsystem converts the optical signal to an electrical one to be processed by the microcontroller.

During field testing, in situ tuning of the antenna sensors is necessary, and a miniature vector network analyzer (VNA, "NanoVNA," 10 KHz–1.5 GHz, SeeSii, China) is inserted into the tuning circuit close to the antenna sensor. The Digicap arrays (Cr/Cm) are tuned to the resonant values on a platform 0.3 m above undisturbed ground (Figure 7). The results of the

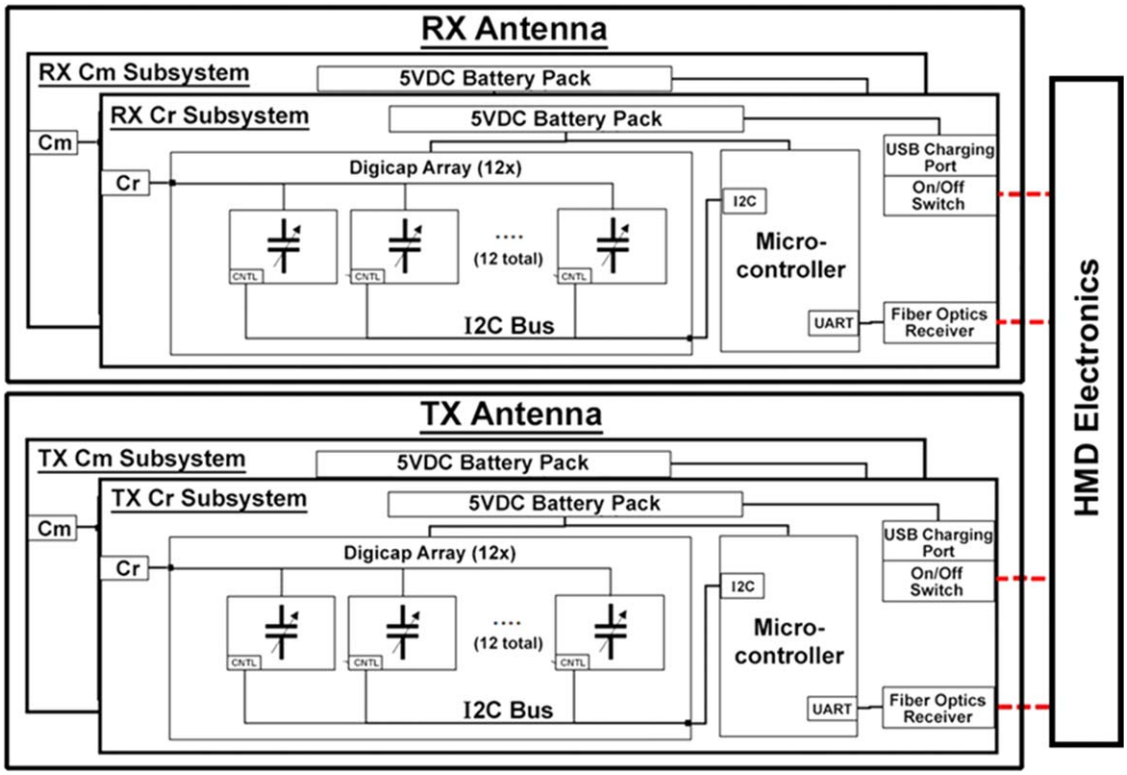

Figure 6. Block diagram for the antenna sensor tuning with arrays of digital programmable capacitor (Digicap NCD2400M × 12) for Cr/Cm. A total of four arrays are used: Rx (Cr subsystem, Cm subsystem), Tx (Cr subsystem, Cm subsystem). The Digicap arrays are placed inside the gray box shown in Figure 4(C) and communicate with the rest of the HMD electronics through optic fibers (indicated in red).

in situ tuning are plotted in Figure 7(B), with S_{11} (reflection coefficient) as a function of HMD frequency.

The S_{11} versus frequency plot is mainly for the purpose of tuning and tracking the antenna sensor elements. In principle, changes in the S_{11} values when the HMD is traversed over a gypsum sample (absorption of RF power) can be regarded as signal, but in practice, the gypsum absorption is so small that it requires a sophisticated signal-processing scheme (Section 2.3) and is never meant to be observed in the S_{11} tuning plots. When the antenna tuning is performed, the data are used as a background for the subsequent signal processing. In an unknown environment, if the tuning is performed over a gypsum deposit, the HMD will detect an inverted signal of gypsum when moved to a gypsum-free site. Thus, the correct gypsum site could be inferred from the phase of the signal.

Figure 7(C) shows a plot of the measured values of $Q(f)$, the antenna sensor quality factor. In general, for resonators (Eaton et al. 2010),

$$Q\alpha\sqrt{f}, \tag{1}$$

in which f is the HMD frequency. Figure 7(C) shows that Q follows Equation (1). In the HMD signal processing (Section 2.3), FM is used with an amplitude of $\pm 3\Delta f$. The FM has a similar effect of averaging for $S_{11}(f)$ and $Q(f)$ as expressed by Equation (2),

$$S_{11}(f)\ \text{average} = [S_{11}(\pm 3\Delta f) + S_{11}(\pm 2\Delta f) + S_{11}(\pm \Delta f) + S_{11}(f)]/7, \tag{2}$$

where the Q average is derived in the same manner. The average values of S_{11} and Q are the ones actually affecting the signal processing.

2.3. HMD Electronics and Signal Processing

During HMD operation, the RF is scanned (0.8–5.4 MHz; tuned range 0.8–4 MHz) in a step size of $\Delta f = 36.22$ kHz with FM ($f_{\text{mod}} = 3.125$ kHz; amplitude $f_{\text{amp}} = \pm 3\Delta$, $\Delta = 36.22$ kHz). To establish a baseline, the extra RF range (4–5.4 MHz) is scanned, where there is a monotonous spectral absorption with a small slope (Figure 1), and this will contribute only a minor perturbation when detected as a derivative signal. The RF scan (0.8–5.4 MHz) takes ~40 s.

The FM frequency and amplitude are software-configurable for optimum signal detection. During the RF scan with FM, the corresponding Cr/Cm values are applied from preprogrammed values to maintain resonance at all times. These tuned capacitance values are predetermined off-line following a set of calibration procedures with a network analyzer.

Functional block diagrams of the HMD electronics and signal-processing circuit are shown in Figures 8–10. For a sweepable frequency source, a direct digital synthesizer (DDS; AD9834, output frequency <37.5 MHz) is used. For signal processing, synchronous detection is used, and signals are extracted by software executed on the microcontroller. The parameters, FM frequency ($F_{\text{mod}} = 200$ or 3.125 kHz), and FM amplitude ($f_{\text{amp}} = \pm 3\Delta, \pm 2\Delta, \pm \Delta$, $\Delta = 36.22$ kHz) all are software-configurable for optimum HMD signals.

To fully characterize the RF absorption by subsurface materials, quadrature detection (0° and 90°, dual MC1496) is used so that the phase and amplitude of the RF absorption can be measured (Figures 9 and 10).

The HMD signal processing uses a lock-in amplifier that is comprised of both IF mixing and low-pass filtering at each

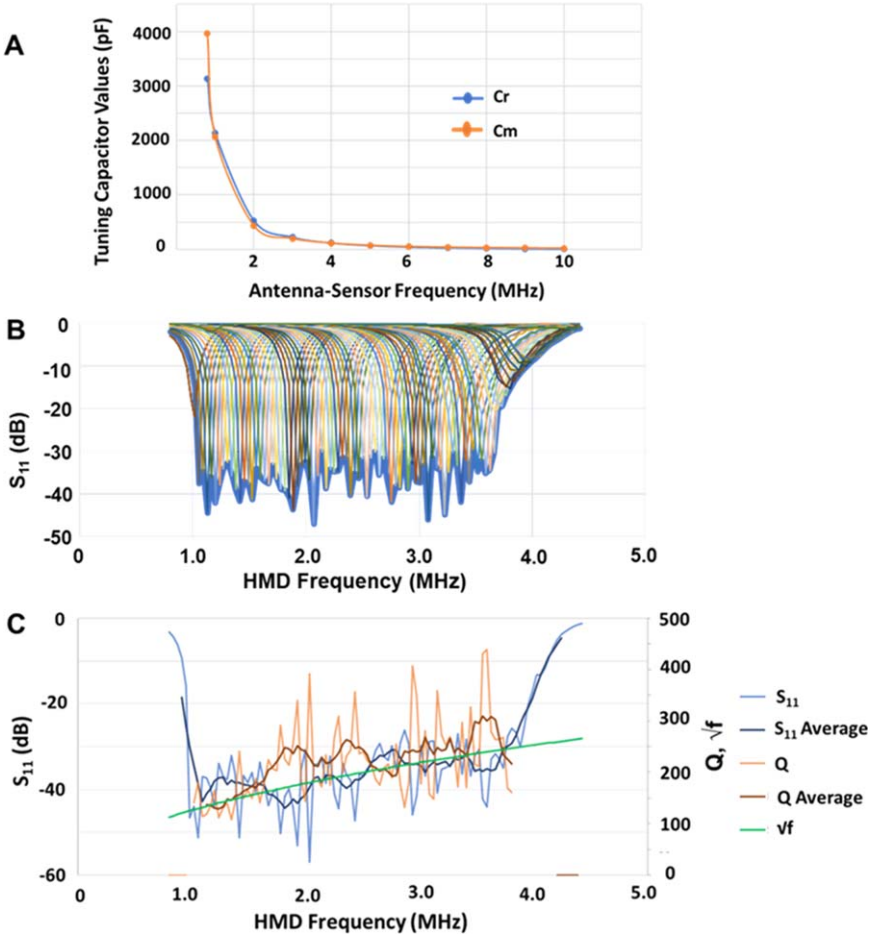

Figure 7. (A) Plot of simulated antenna sensor tuning capacitor values (Table 1) Cr and Cm for the frequency scan ranges of 0.8–10 MHz with discrete sets of capacitors in the laboratory. (B) Digicap array (Cr/Cm) tuning with in situ VNA. Shown are plots of S_{11} vs. HMD frequency with steps of $\Delta f = 36.22$ kHz at the field site 0.3 m above undisturbed ground without gypsum. The thick blue curve traces the S_{11} envelope. (C) Plots of S_{11}(dB), S_{11} average, Q, and Q average vs. HMD frequency. Shown is a plot of the Q average trends with Equation (1) (green). The HMD antenna sensor tuned frequency range is Tx/Rx 0.8–4 MHz.

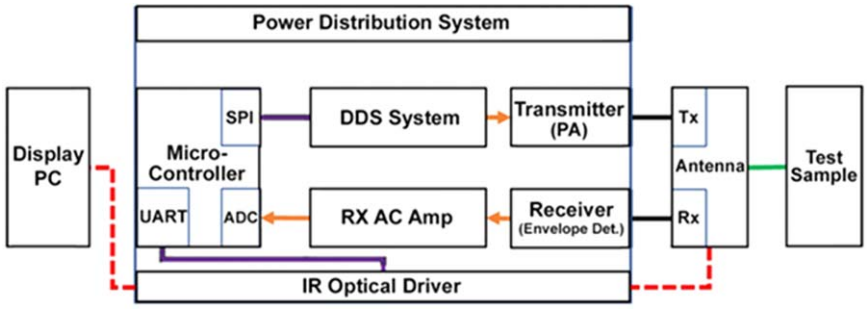

Figure 8. Functional block diagram for the HMD system electronics. Components include: Power Distribution System (DC/DC Converter [V_{in} = 5–9 VDC, V_{out} = 3.3, ±12 VDC] and additional low-drop out regulators for improved noise rejection); Micro-controller (IMXRT1062DVL6 [600MHz 32-bit ARM Processor with integrated peripherals such as analog-to-digital converter (ADC), serial peripheral interface (SPI), Universal Asynchronous Receiver Transmitter (UART), general-purpose input/output (GPIO), and timers]); Direct Digital Synthesizer (DDS) System (AD98348 [0.8–10 MHz], RF sweep between 0.8 MHz – 5.4 MHz with programmable frequency modulation [Fmod = 200 Hz or 3.125 kHz] controlled by the Micro-controller); Transmitter power amplifier (PA) (ZX60-100VHX+ [1W RF amplifier] with inline 10 dB attenuator); Receiver (AD8307 [Envelop detector with sensitivity down to –75 dBm between DC-500 MHz]); RX AC amp (LT1225 op-amp [30 dB small signal gain]); IR Optical Driver (IR LED [Data is out to a lap-top PC via infrared optical fiber over UART interface]); Display PC (The control and data storage/processing of the HMD are achieved by a laptop PC); Antenna (The output of the Transmitter PA is connected to the TX antenna element via a RF SMA interface and the input of the Receiver is connected to the RX antenna element via a RF SMA interface).

frequency point by a simple boxcar average filter. Such a low-pass filter is implemented in the embedded controller firmware. The integration time associated with the low-pass filter algorithm is where most of the scan time (∼40 s) is allocated. With an improved low-pass filter algorithm (higher filter order and optimal filter selection), one can further reduce the integration time, suitable for a continuous traverse scan mode (Section 3). Higher filter order design, such as cascaded integrator-comb filters (Hogenauer 1981), can be employed for an improved filter response. An edge detection algorithm will be able to enhance the signal by constantly updating the background and performing background removal in real time.

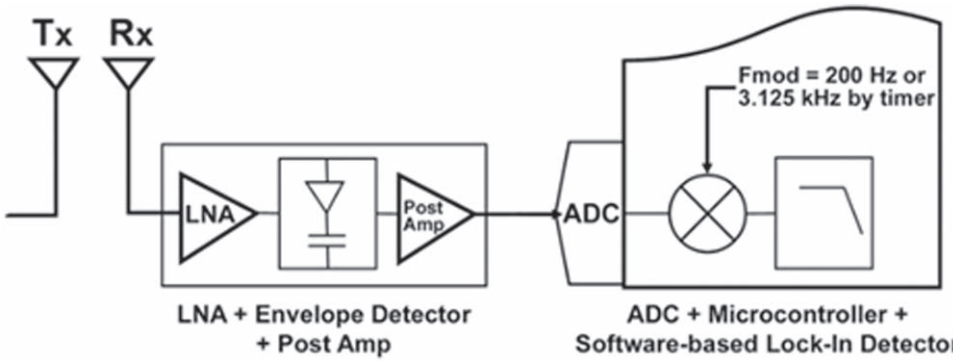

Figure 9. HMD receiver (Rx) functional block diagram for electronic signal processing. Low noise amplifier (LNA) followed by envelope detection. The carrier-removed signal is further enhanced by the post amplifier, providing gain and dc biasing suitable for the subsequent analog-to-digital converter (ADC) stage. The digitized signal is then mixed with FM frequency, 3.125 kHz (or 200 HZ), then low-pass filtered for lock-in detection.

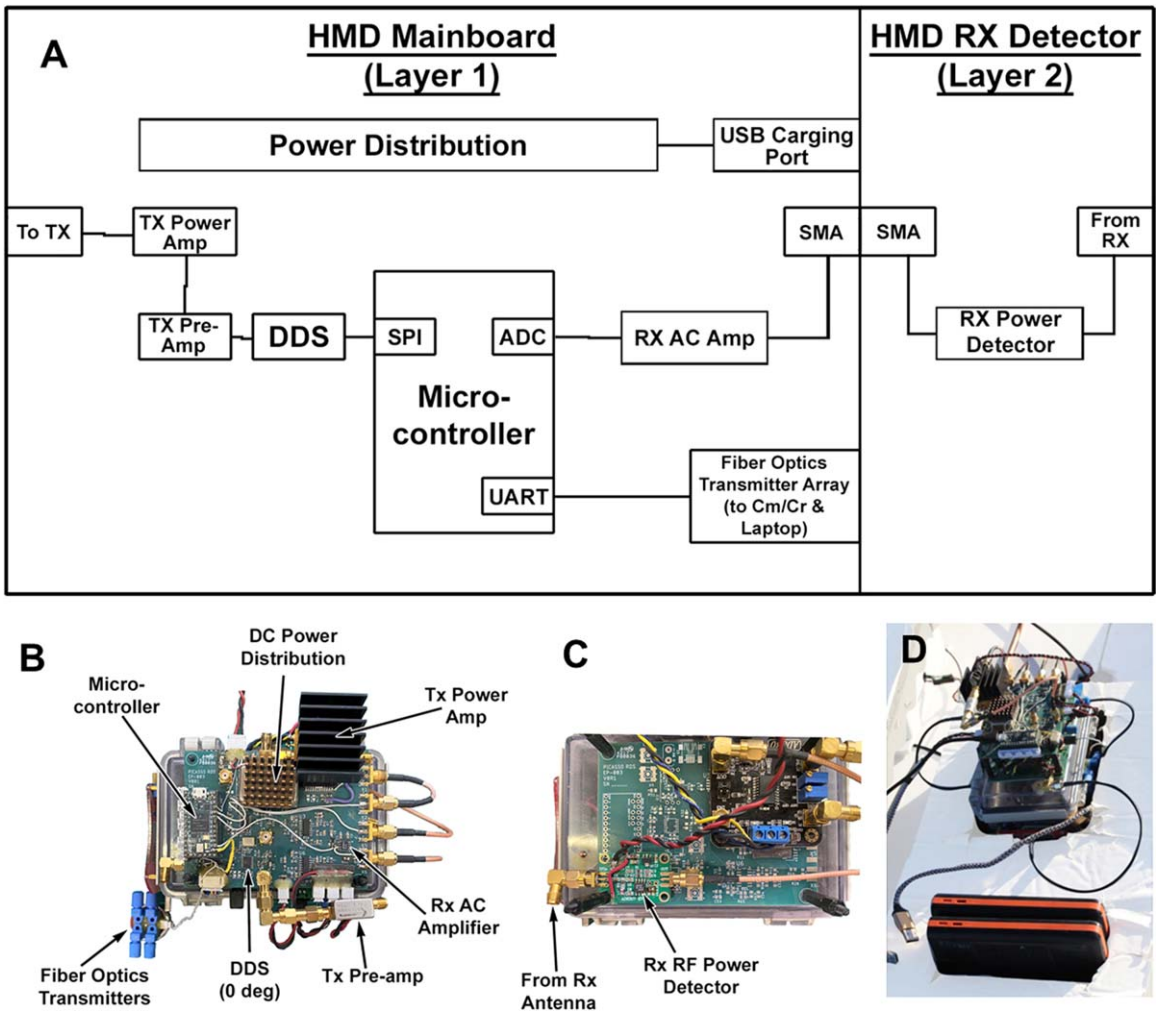

Figure 10. HMD electronics. Panel (A): Functional block diagram for two electronic boards, Layer 1 and Layer 2. Panel (B): Layer 1 (HMD main board). The components include: DC Power Distribution System (DC/DC Converter [$V_{in} = 5$–9 VDC, $V_{out} = 3.3, \pm 12$VDC] and additional low-drop out regulators for improved noise rejection); Micro-controller (IMXRT1062DVL6 [600MHz 32-bit ARM Processor with integrated peripherals such as analog-to-digital converter (ADC), serial peripheral interface (SPI), Universal Asynchronous Receiver Transmitter (UART), general-purpose input/output (GPIO), and timers]); Direct Digital Synthesizer (DDS) System (AD98348 [0.8–10 MHz], RF sweep between 0.8 MHz – 5.4 MHz with programmable frequency modulation [Fmod = 200 Hz or 3.125 kHz] controlled by the Micro-controller); Transmitter power amplifier (PA) (ZX60-100VHX+ [1W RF amplifier] with inline 10 dB attenuator); RX AC amp (LT1225 op-amp [30dB small signal gain]); IR Optical Driver (IR LED [Data is out to a laptop PC via infrared optical fiber over UART interface]); Display PC (The control and data storage/processing of the HMD are achieved by a laptop PC). Panel (C): Layer 2 (HMD Rx detector). Receiver (AD8307 [Envelop detector with sensitivity down to −75dBm between DC-500 MHz]); Antenna (the input of the Receiver is connected to the RX antenna element via a RF SMA interface). Panel (D): Assembled HMD electronics. The two boards (Layers 1 and 2) are stacked. The HMD electronics with a battery pack are placed between the Tx/Rx antenna-sensors on the moving platform during field testing (Figure 4C).

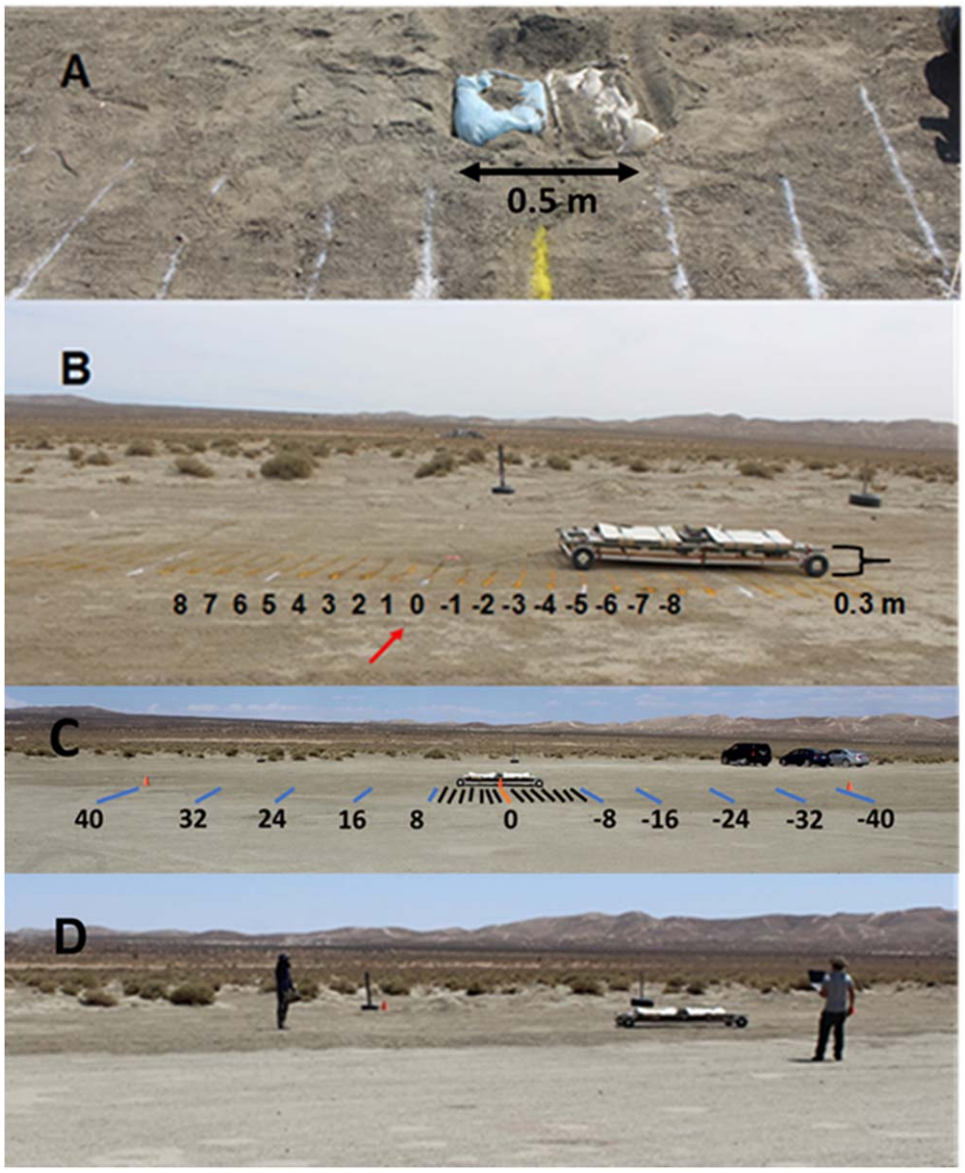

Figure 11. Field testing at El Mirage Dry Lake Bed, CA. (A) Picture showing two bags of samples [gypsum (20 kg × 2) or sand (22 kg × 2)] before burial. (B) The two bags of gypsum or sand are buried sequentially at the same spot (position 0), 2–3 cm soil on top, flush to the ground. (D) The moving platform with the HMD (0.3 m above the ground) was pulled by hand through a rope (10 m long) over each marked distance interval (fine, 0.3 m (1′), as shown in panel (B); or coarse, 2.4 m (8′), as shown in panel (C)). When moved to a new position, it paused for ∼40 s for the system to settle down from the motion, and then data were taken by scanning the RF from 0.8 to 5.4 MHz in ∼40 s. To reduce vibration during traverse, plastic foams (4 each, 0.5 m × 1 m each) were used to cover the antenna sensors. A laptop PC was used for controlling and collecting data through a 10 m long optical fiber.

Operation of the HMD instrument is autonomous per its default parameters but designed to be configurable and able to respond to other testing and calibration commands. Upon powering on of the HMD electronics, RF scanning starts automatically. Each spectrum consists of 128 frequency points (128 × 36.22 kHz frequency steps = 4.6 MHz, scan range from 0.8 to 5.4 MHz), and each frequency point is a 64-bit integer (8 bytes) representing the signal level. Therefore, the data size of each spectrum is 1024 bytes, i.e., 1 kB.

Currently, the spectral data are first postprocessed by embedded electronics and then transmitted to the graphical user interface (GUI) processing computer via an optical channel. As soon as the GUI application receives the spectral data, minimal processing is needed to depacketize, store to memory, and update the graphical display, all of which is completed within 40 ms after the receipt of the spectral data.

3. Field Testing

3.1. Field Testing

As shown in Figure 11, a moving platform was used during the field testing. The platform is made of PVC pipe [3.175 cm diameter (1.″25 diameter), 3 m (L) × 1 m (W)] with four plastic wheels at a height of 0.3 m from the ground. The antenna sensors (Tx/Rx) are placed on top of the platform with HMD electronics in between the antenna sensors (Figure 4).

The antenna sensors are covered by plastic foams (4 each, 0.5 m × 1 m each), and the moving platform was supported by fiberglass rods (two each of 90° angles + two each of U channels, all 3 m long) and weighted with two pieces of lumber (two each of 5 cm × 10 cm × 3 m). The moving platform was pulled by hand through a rope (10 m long) over each marked distance as shown in Figure 11. During the field scan, the HMD

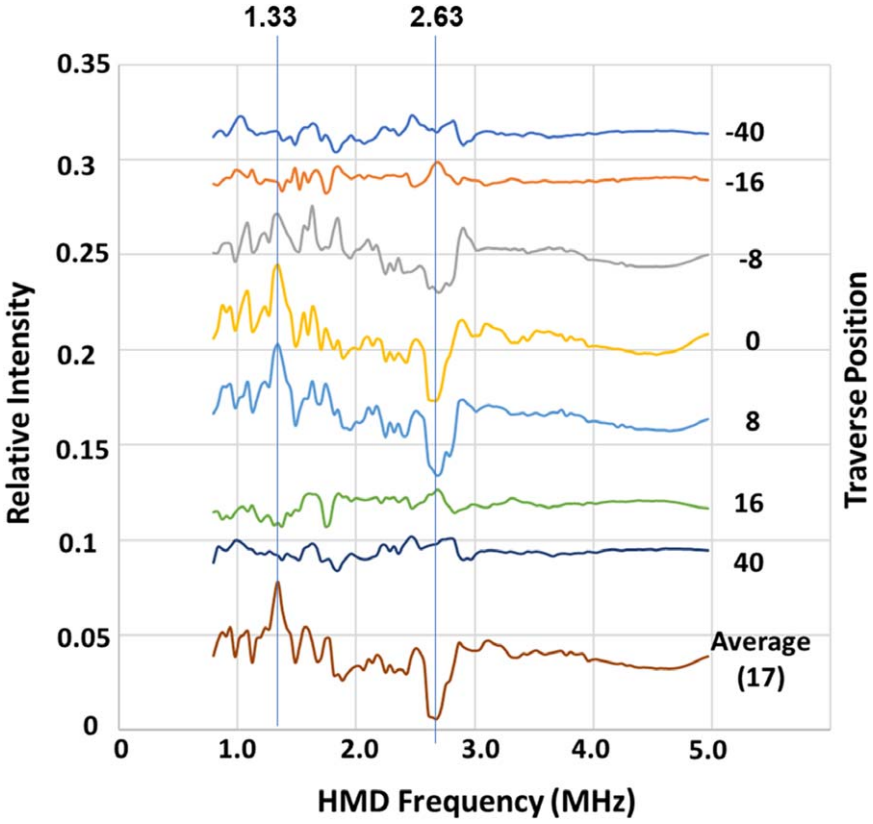

Figure 12. The HMD spectra of gypsum after background subtraction (RG–BS) from El Mirage field testing. The HMD was traversed from position −40 to +40 (coarse scan), stepped through 2.4 m distance. The samples, gypsum or BS, were buried sequentially at position 0. All of the data were taken while the HMD platform was stationary. The bottom spectrum (average 17) was obtained from an average of 17 gypsum data from −8 to +8 (fine scan). The resultant gypsum signal is shown as a derivative of absorption, peak at 1.33 MHz, valley at 2.63 MHz, at positions −8, 0, and 8 and also the average of 17 fine scans.

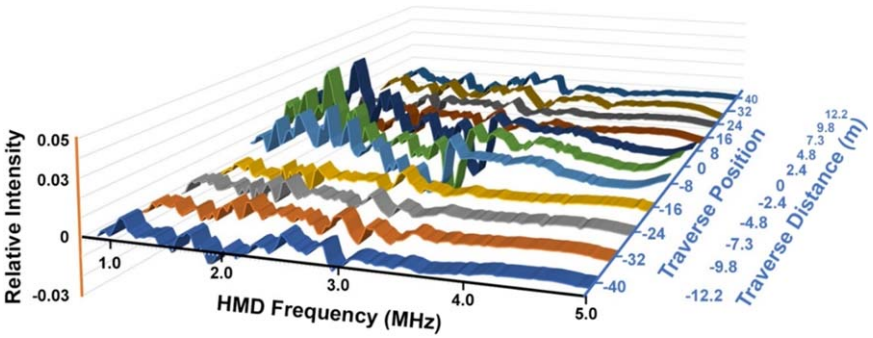

Figure 13. A 3D plot of HMD gypsum spectra (RG–BS) from El Mirage field testing (Figure 11). The HMD was traversed from position −40 to +40 (coarse scan), stepped through 2.4 m traverse distances. Notice the gypsum signal from −8 to 8; the gypsum sample or BS was buried sequentially at position 0.

was communicated with using a laptop PC through an optical fiber connection.

The light weight of the moving platform (∼10 kg), as well as the uneven speed of hand pulling (subject to acceleration/deceleration), makes the HMD system prone to vibration during traversing. To reduce vibration-induced artifacts, the tests were done in a stop-and-go manner; i.e., the moving platform was pulled to a spot and then paused for an ∼40 s settling time, then commanded to take data (a 0.8–5.4 MHz scan for ∼40 s), then moved to the next spot, etc.

The HMD spectrometer was field tested at El Mirage Dry Lake Bed, Adelanto, CA (Figure 11). As for the samples, two bags of gypsum (20 kg × 2, Alpha Chemicals, $CaSO_4 2H_2O$) or two bags of sand (BS; 22 kg × 2, control) were buried sequentially at the same spot (position 0), with 2–3 cm soil on the top, flush to the ground.

The BS were used as a control to compensate for possible artifacts from ground disturbances caused by the digging and presence of plastic container bags. Thus, the physical conditions of the buried samples (gypsum or sand) were similar. To reduce any effects from the local characteristics of the ground, the gypsum or sand samples were buried sequentially at the same spot (position 0) in the ground as the field testing progressed. For example, the gypsum was buried first (position 0), and HMD scan data were acquired from 17 positions (from position −8 to 8, −2.4 to +2.4 m, at 0.3 m intervals, fine sample scan); then BS were buried at the same spot (position 0), HMD scan data were acquired again

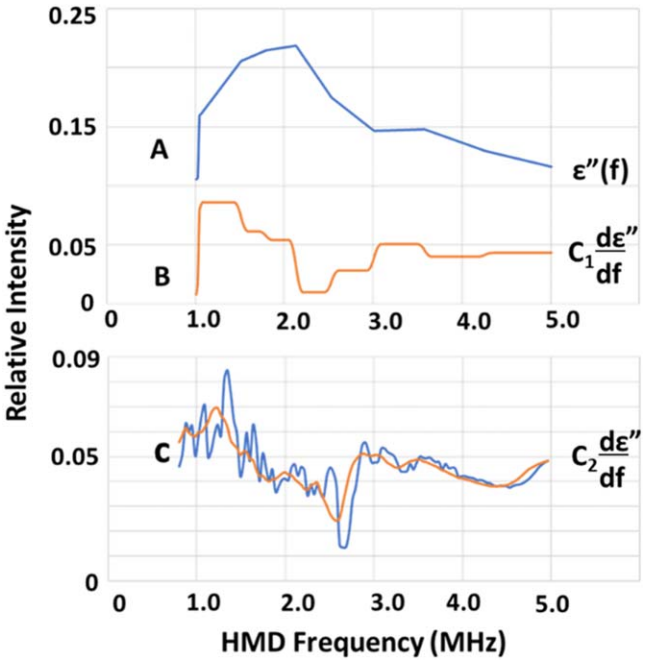

Figure 14. Comparison of gypsum spectra. (A) Gypsum absorption spectrum, $\varepsilon''(f)$, from a laboratory dielectric spectrometer (Figure 1(C)). (B) Derivative of gypsum absorption spectrum, $c_1 d\varepsilon''/df$. (C) The blue line shows the gypsum spectrum obtained by the HMD (Figure 12 at zero traverse position) overlapped with the numerically filtered version (orange line; average of $(\pm 3\Delta f)$). The HMD uses FM $(\pm 3\Delta f)$ for signal processing, and the resulting spectrum is in the derivative form; it matches (B). Here C_1 and C_2 are proportionality constants.

from 17 positions (from −8 to 8, fine background scan), etc. Coarse scans (from position −40 to +40, −12.2 to 12.2 m, at 2.4 m intervals, 11 positions) were also made in the same manner, sequentially burying gypsum and sand at position 0. For the fresh ground (FG), the background scan data were taken first; then bags of gypsum or sand samples were buried sequentially at the same spot (position 0) to obtain the rest of the HMD data.

All of the gypsum absorption spectra were obtained by subtracting corresponding backgrounds (BS or FG) from the raw gypsum (RG) data.

HMD parameters used. The HMD total system power required is ∼5 W, FM frequency is 3.125 kHz, FM amplitude is $\pm 3\Delta f$ (±108.66 kHz), scan time is ∼40 s (0.8 MHz–5.4 MHz)/scan, and RF power (Tx output) is 10 mW. The RF generated in the HMD system (1 W) was attenuated 20 dB at the Tx output side to avoid burning out the Digicap array. The scan made during the move to the next position was discarded; then, after settling down (∼40 s), one scan at each position was saved as data.

3.2. Results and Discussions

The HMD spectra of the buried gypsum sample (buried position 0; Figure 11) from the fine scan (position −8 to 8) and the coarse scan (position −40 to +40) after subtraction of the respective backgrounds (RG–BS) are shown in Figures 12 and 13. The background subtraction, e.g., RG–BS or RG–FG, showed little difference for the gypsum signal. It seems that artifacts from digging or the presence of plastic bags can be ignored. However, background subtraction is necessary to compensate for the inherent antenna sensor frequency dependence. Considering the buried sample width of 0.5 m, the HMD horizontal resolution is ∼2 m at a shallow depth.

Figure 14 shows a comparison of gypsum spectra (Figure 1) obtained from a laboratory dielectric spectrometer ((A), absorption $\varepsilon''(f)$; (B), derivative of absorption, $d\varepsilon''/df$) and gypsum spectrum obtained by HMD (C). Since FM is used for signal processing, HMD shows the derivative spectrum, $d\epsilon''/df$, of gypsum absorption, $\epsilon''(f)$, and matches spectrum B. The numerically filtered spectrum C (orange) was obtained in the same manner as described in Equation (2).

3.3. RF Interference Concerns

With any RF instrument, including the HMD and ground-penetrating radar (GPR), there have been concerns regarding mutual RF interference with other instruments or the metallic rover body under a deployment scenario.

Those concerns can be mitigated by signal processing. Since the interference with the rover body is always present (periodic, or not changing), it can be dealt with as a background and subtracted through a signal-processing algorithm (e.g., filter in frequency domain). Thus, changes from the background can be treated as signal. Also, interference from the rover body is over a short distance and can be gated out by a time delay during data collection (time gating).

From past experience with GPR deployment on the Athlete rover (Figure 15), the concept has been tested and proved. The interference from the rover body was filtered out by a combination of background subtraction and time gating. Remote commands for Athlete rover operation and the RF pulse from the GPR did not interfere with each other (separation in frequency).

For the case of the Mars Perseverance rover (Mars 2020), the GPR named Radar Imager for Mars' subsurFAce eXperiment (Hamran et al. 2020) is utilizing the metallic rover body as a part of the antenna structure. However, due to the resonance tuning requirements of the antenna sensor, this application is not for the HMD instrument. The resonance tuning of HMD antenna sensors could be calibrated with the presence of the metallic rover as part of an in situ tuning process.

4. Conclusions

A rover-mounted HMD demonstrated the detection of shallow buried hydrated minerals, e.g., gypsum, while mounted on a moving platform (0.3 m above ground) without any sample preparation. Extra efforts were made to remove artifacts by subtraction of the background from the raw gypsum data. The HMD is the first of its kind, unlike conventional laboratory dielectric spectrometers that require small amounts of samples (5–10 g) to be placed inside sample cells. Through field testing, the HMD instrument proved the concept of detection of buried hydrated minerals by scanning over the surface. Currently, the HMD instrument is at TRL 4.

For field testing, the "stop-and-go" method was used to confirm the detection capabilities of the HMD for the presence of gypsum with spectral features (a derivative of absorption, peak at 1.33 MHz, valley at 2.63 MHz), as well as to minimize vibration-induced artifacts.

Compared with the HMD field testing method used, i.e., uneven hand pulling (prone to acceleration/deceleration), as well as a low-mass moving platform (10 kg), the Mars rovers, e.g., Perseverance $<\sim 2\,\mathrm{m\,minute^{-1}}$, dry mass = 1025 kg or

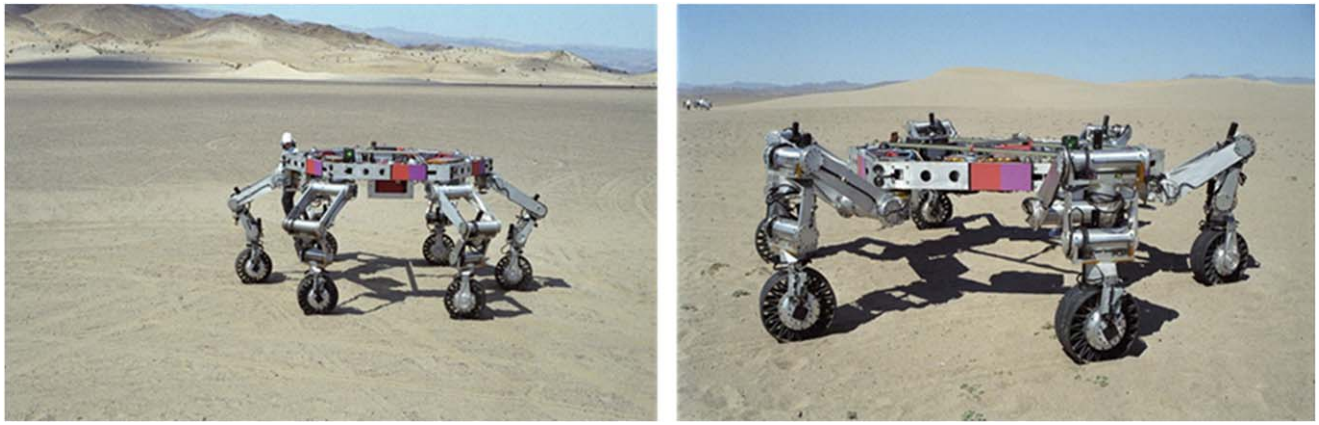

Figure 15. GPR on Athlete rover during field testing at Dumont Dunes, CA, 2006 June 13.

Table 2
HMD Instrument Summary

RF scan range (RF tuned range)	0.8–5.4 MHz (0.8–4 MHz)
RF scan time	~40 s
Data volume/spectrum	1 kB
Horizontal resolution	2 m
RF output power (Tx)	0.01 W
HMD total system power	5 W
HMD instrument weight	1.5 kg
Current TRL	4

Curiosity <0.3 m minute^{-1}, 900 kg, have a slow mechanized speed, e.g., ~ 0.3 m minute^{-1}, and much higher mass ($\sim$100 times). Thus, the Mars rovers will present little vibration for the performance of HMD. The HMD could be deployed in a continuous traverse manner using differential detection that continuously subtracts previous scan averages as background from current data. This way, the HMD will show a peak (or valley) at the edges of the gypsum encounter, as well as a valley (or peak) when it leaves the gypsum site, i.e., so-called "edge detection." Thus, at the nominal speed of the Mars rovers (~ 0.3 m minute^{-1}), the HMD will have enough time for the detection and signal processing in situ along the traverse.

The HMD instrument summary is given in Table 2. The HMD instrument could be further developed to TRL 6 through a next-level NASA instrument development program such as MATISS.

The original plan was to develop the HMD instrument with wider frequency scan ranges, i.e., 0.8–10 MHz, which would help to obtain a steady baseline for the detection of hydrated minerals. However, due to the limitations in commercially available off-the-shelf (COTS) electronically tunable capacitors, e.g., Digicap, the HMD resonance tuned scanning range is limited to 0.8–4 MHz (RF scan range 0.8–5.4 MHz), with the transmit RF power attenuated to 0.01 W, even though the HMD produces full 1 W RF power. Future availability of COTS digital programmable capacitors that can cover the wider frequency ranges, e.g., 0.8–10 MHz, as well as operate at higher voltage ranges, e.g., 10 V, will make the HMD with full transmit frequency and power. The full RF power (Tx = 1 W) could have produced a more robust HMD spectrometer in signal quality and sensitivity.

The CST simulation plot (Figure 4(D)) shows that with a Tx power of 1 W, the electric field, E, is 0.3 V m^{-1} at <1 m depth, 0.03 V m^{-1} at ~ 2 m depth, and 0.005 V m^{-1} at 4 m depth. The HMD field testing used 0.01 W RF power for the detection of gypsum samples at a shallow depth, <1 m. According to the relationship shown in Equation (3),

$$E \alpha \sqrt{P_{\rm rf}}, \text{ in which } P_{\rm rf} = \text{RF power}, \quad (3)$$

the E field used for the detection of gypsum is $E = 0.03$ V m^{-1} at 0.01 W RF power. At the full RF power of 1 W, this corresponds to the E field at ~ 2 m depth into the soil. From the point of E field strength, the HMD could potentially detect hydrates down to 2 m depth ($P_{\rm rf} = 1$ W) or with increased RF power, e.g., $P_{\rm rf} = 36$ W, down to 4 m depth (0.005 V m^{-1} $\times \sqrt{36} = 0.03$ V m^{-1}) into Martian soil.

To achieve the higher RF power (1 or 36 W), one needs a relevant power amplifier, as well as antenna sensor tuning elements that can withstand the required higher voltage corresponding to the higher RF power. The HMD can utilize COTS power amplifiers. However, for the tuning elements, the voltage rating of the digital programmable capacitors (Digicap), e.g., NCD2400M ($\leqslant$3.3 V), must be higher than the transmitter RF voltages by a sufficient margin. For example, the transmitter with 1 W RF power (30 dBm) in a 50 ohm system, the Digicaps are subject to 7 Vrms (or 20 Vp-p), which is beyond the specified limits. Current HMD design uses the Digicaps in a parallel configuration (Figure 6) at an RF power of 10 mW (10 dBm, 3.3 V). However, the same design will not withstand the voltage at 1 W RF power (30 dBm or 20Vp-p) or 36 W (45.6 dBm or 120Vp-p). The current Digicap design can be improved to withstand the transmitter voltages by instantiating multiple parallel Digicap arrays (m Digicaps in parallel) and connecting them in series (n Digicap arrays in series), a total of $m \times n$ Digicaps, for the Cr and Cm, respectively. This approach, though very complex, can increase the equivalent voltage rating of the entire network while maintaining the dynamic range and controllability of the Digicap network.

As for future deployment on Mars, the HMD antenna sensors, which are two loops of copper tube (0.635 cm OD $\times$ 0.483 cm ID, 1 m $\times$ 1 m each; Figure 2), could be deployed on the underside of the Mars rover. Alternately, the antenna sensors could be mounted on a sturdy fiberglass frame

attached to the rover through hinge mechanisms that can be folded/stowed (1 m × 1 m), then deployed out (1 m × 2 m) on the backside or one side of the rover (0.3–1 m height from ground) during data taking.

Under previous NASA instrument development programs (PIDDP (2000–2002), MIDP (2003–2005), PI: S. S. Kim), miniature GPRs (impulse radars (center frequency at 800 and 80 MHz); Kim et al. 2002, 2006) have been developed. A combined HMD and GPR can be mounted on a rover and obtain the presence of hydrated minerals with stratigraphy information.

The research described in this publication was carried out at the Jet Propulsion Laboratory, California Institute of Technology, under a contract with the National Aeronautics and Space Administration (NASA). The work was financially supported by the NASA instrument development program, PICASSO (2017–2020). Assistance by Yasmin Shri and Jamie Daniels, both Caltech graduate students at the beginning of this project, is acknowledged. Reference herein to any specific commercial product, process, or service by trade name, trademark, manufacturer, or otherwise does not constitute or imply its endorsement by the United States Government or the Jet Propulsion Laboratory, California Institute of Technology. The authors declare no competing financial interest.

Appendix

Below is a list of abbreviations used in this paper.

List of Abbreviations

AC = Alternating Current
ADC = Analog-to-Digital Converter
CheMin = Chemistry & Mineralogy
CIC = Cascaded Integrator-Comb
CRISM = Compact Reconnaissance Imaging Spectrometer for Mars
CST = Computer Simulation Technology
DC = Direct Current
DDS = Direct Digital Synthesizer
Digicap = digital programmable capacitor
E = Electric field
EM = Electromagnetic
ESA = European Space Agency
FM = Frequency Modulation
GEL = Global Equivalent Layer
GPIO = General Purpose Input/Output
GPR = Ground Penetrating Radar
H = Magnetic field
HFSS = High Frequency Structure Simulator
HMD = Hydrated Mineral Detector
I2C (or I^2C) = Inter-Integrated Circuit
LNA = Low Noise Amplifier
IR = Infrared
ISRU = In Situ resource Utilization
LC = inductor capacitor
MARSIS = Mars Advanced Radar for Subsurface and Ionospheric Sounding
MEO = Mars Express orbiter (ESA, 2003)
MER = Mars Exploration Rover
Mini-TES = Miniature Thermal Emission Spectrometer
MRO = Mars Reconnaissance Orbiter
MSL = Mars Science Laboratory
NASA = National Aeronautics and Space Administration
OMEGA = Observatoire pour la Mineralogie, l'Eau, les Glaces, et l'Activité
PA = Power Amplifier
PVC = Polyvinyl Chloride
Q = Quality factor
RF = Radio Frequency
RIMFAX = Radar Imager for Mars' Subsurface Exploration
Rx = Receive
S_{11} = reflection coefficient
SAM = Sample Analysis at Mars
SHARAD = Shallow Subsurface Radar
SPI = Serial Peripheral Interface
TRL = Technology Readiness Level
Tx = Transmit
UART = universal Asynchronous Receiver Transmitter
VDC = Voltage Direct Current

References

Abbud-Madrid, A., Beaty, D. W., Boucher, D., et al. 2016, Mars Water In-Situ Resource Utilization (ISRU) Planning (M-WIP) Study, http://mepag.nasa.gov/reports/Mars_Water_ISRU_Study.pptx
Allen, C. C., Jager, K. M., Morris, R. V., et al. 1998, EOSTr, 34, 405
Allwood, A. C., Burch, I. W., Rouchy, J. M., & Coleman, M. 2013, AsBio, 13, 870
Arvidson, R. E., Poulet, F., Bibring, J.-P., et al. 2005, Sci, 307, 1591
Balci, N., Gunes, Y., Kaiser, S. A., et al. 2020, Geomicrobiol. J., 37, 401
Bellett, P. T., & Leat, C. J. 2003, in IEEE Antennas and Propagation Society International Symp., Vol. 2 (Piscataway, NJ: IEEE), 235
Bibring, J. P., Langevin, Y., Gendrin, A., et al. 2005, Sci, 307, 1576
Blake, D. F. & the MSL Science Team 2013, LPSC, 44, 1289
Boswell, A., Tyler, A. J., & White, A. 2005, ITAP, 47, 51
Boynton, W. V., Bailey, S. H., Hamara, D. K., et al. 2001, JGRE, 106, 17683
Cámara, B., Souza-Egipsy, V., Ascaso, C., et al. 2016, ChGeo, 443, 22
Christensen, P. R., Wyatt, M. B., Glotch, T. D., et al. 2004, Sci, 306, 1733
Dong, H., Jiang, J. A., Sun, H., & Buck, B. J. 2007, JGRG, 112, G02030
Dubrovkin, J. 2021, Derivative Spectroscopy (Newcastle upon Tyne: Cambridge Scholors Publishing)
Eaton, G. R., Eaton, S. S., Barr, D. P., & Weber, R. T. 2010, Quantitative EPR (Dordrecht: Springer), 79
Gendrin, A., Mangold, N., Bibring, J. P., et al. 2005, Sci, 307, 1587
Grum, F., Paine, D., & Zoeller, L. 1972, ApOpt, 11, 93
Hamran, S.-E., Paige, D. A., Amundsen, H. E. F., et al. 2020, SSRv, 216, 128
Hogenauer, E. 1981, ITASS, 29, 155
Jensen, M. A., & Rahmat-Samii, Y. 1994, ITAP, 42, 264
Kim, S. S., Carnes, R., Mysoor, N. R., Ulmer, C. T., & Arvidson, R. E. 2002, Proc. SPIE, 4758, 1
Kim, S. S., Carnes, S. R., Haldemann, A. F., et al. 2006, in Paper No. 1365, 2006 IEEE Aerospace Conf. (Piscataway, NJ: IEEE), 4
Klingelhöfer, G., Morris, R. V., Bernhardt, B., et al. 2004, Sci, 306, 1740
Kraus, J. D. 1988, Antennas (2nd ed.; New York: McGraw-Hill), 410
Langevin, Y. F., Poulet, J. P., Bibring, B., & Gondet, B. 2005a, Sci, 307, 1584
Langevin, Y. F., Poulet, J. P., Bibring, B., et al. 2005b, Sci, 307, 1581
Mahaffy, P. R. & the MSL Science Team 2013, LPSC, 44, 1395
Meakins, R. J. 1961, Prog. in Dielectrics, Vol. 3 (New York: Wiley), 151
Morris, R. V., Ming, D. W., Clark, B. C., et al. 2005, LPSC, 36, 2239
Mustard, J. F., Murchie, S. L., Pelkey, S. M., et al. 2008, Natur, 454, 305
Mustard, J. F., Poulet, F., Gendrin, A., et al. 2005, Sci, 307, 1594
Oren, A., Sørensen, K. B., Canfield, D. E., et al. 2009, HyBio, 626, 15
Pan, L., Ehlmann, B. L., Carter, J., & Ernst, C. M. 2017, JGRE, 122, 1824
Schopf, J. W., Farmer, J. D., Foster, I. S., et al. 2012, AsBio, 12, 619
Stivaletta, N., & Barbieri, R. 2009, in From Fossils to Astrobiology. Cellular Origin, Life in Extreme Habitats and Astrobiology, Vol. 12, ed. J. Seckbach (Dordrecht: Springer), 319
Vaniman, D. T., Bish, D. L., Chipera, S. J., et al. 2004, Natur, 431, 663
Vítek, P., Ascaso, C., Artieda, O., & Wierzchos, J. 2016, Anal. Bioanal. Chem., 408, 4083
Wernicke, L. J., & Jakosky, B. M. 2021, JGRE, 126, e06351
Wierzchos, J. C., Ascaso, C., & McKay, C. P. 2006, AsBio, 6, 415